Topics in Catalysis (2018) 61:875–888
https://doi.org/10.1007/s11244-018-0936-z

ORIGINAL PAPER

Hydrogen evolution in the photocatalytic reaction between methane and water in the presence of CO_2 on titanate and titania supported Rh and Au catalysts

Balázs László[1] · Kornélia Baán[1] · Albert Oszkó[1] · András Erdőhelyi[1] · János Kiss[3] · Zoltán Kónya[2,3]

Published online: 13 April 2018

Abstract

The photocatalytic transformation of methane-water mixture over Rh and Au catalysts supported on protonated (H-form) titanate nanotube (TNT) was investigated. The role of the catalyst structure was analyzed using titania reference support. Furthermore the effect of carbon-dioxide addition was also investigated. The catalysts were characterized by high resolution transmission electron microscopy and X-ray photoelectron spectroscopy (XPS). Photocatalytic tests were performed with a mercury-arc UV source illuminating a continuous flow quartz reactor which was attached to a mass spectrometer. The surface of the catalysts was analyzed by diffuse reflectance infrared spectroscopy during the photoreactions. The changes of the catalysts due to photocatalytic usage were investigated by XPS and temperature programmed reduction methods as well. Most of the methane was generally transformed to hydrogen and ethane, and a small amount of methanol was also formed. The carbon dioxide addition enhanced the rate of the photocatalytic transformation of methane on Rh/TNT with increasing the lifetime of the electron–hole pairs. Bigger gold particles with mainly plasmonic character were more active in the reactions due to the photo induced activation of the adsorbed water. Surface carbon deposits were identified on the catalysts after the photoreactions. More oxidized carbon formed on the Au-containing catalysts than on the ones with Rh.

Graphical Abstract

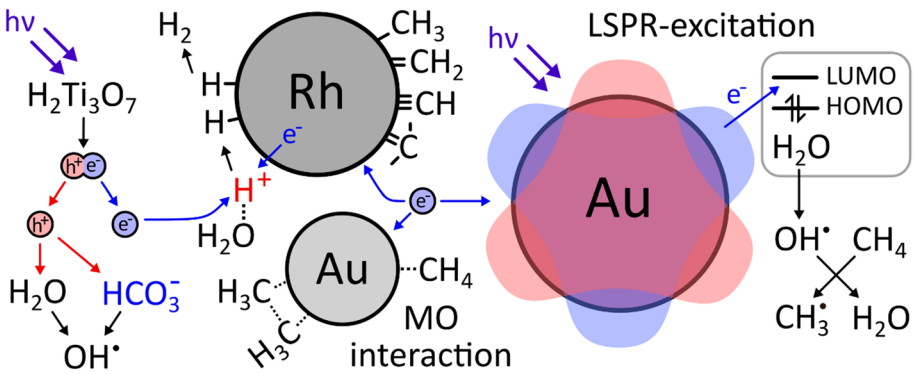

Keywords Heterogeneous photocatalysis · Titanate nanotube · Gold nanoparticle · Molecular-like cluster · Surface plasmon resonance

✉ János Kiss
jkiss@chem.u-szeged.hu

✉ Zoltán Kónya
konya@chem.u-szeged.hu

Extended author information available on the last page of the article

1 Introduction

It is envisaged that in the near future a hydrogen economy will be developed, in which H_2 as the principal energy carrier may replace fossil fuels [1, 2]. The methods for

the effective production, transport and storage of hydrogen are topics of investigation all over the world. As a first approximation water could be the number one candidate as a source for hydrogen production. The pioneering work of Fujishima and Honda in 1972 accelerated the research in the field of water splitting [3]. They achieved UV light induced water splitting using a TiO_2 photoanode and a Pt counter electrode immersed in an electrolyte solution. Since that time the photocatalysis with TiO_2 has attracted significant attention because of its promising application in solar energy conversion [4–8]. The photocatalytic water splitting is a promising option to generate hydrogen if the usage of carbon containing materials needs to be avoided. This method had been widely investigated over the past decades, but, unfortunately, the stability or activity of all the semiconductor photocatalysts reported to date for direct water splitting is too low to justify industry uptake [9, 10]. Therefore the current hydrogen production method is focused on the steam reforming of methane combined with water–gas shift reaction [11, 12].

Methane and carbon-dioxide are both greenhouse gases; their atmospheric concentrations are showing monotonic increase in the past few decades due to human activity. The increased emission rate of these gases, especially of CO_2, contributes to global warming [13]. The dry reforming of CH_4 with CO_2 results in valuable syngas; this would solve the problem if atmospheric or byproduct CO_2 could be used in the reaction [14–20]. Unfortunately, the energy demand of this process is too high to be economical, furthermore, the catalysts easily deactivate at the required temperature [21]. Photocatalysis is a promising way to break the thermodynamic barrier of this endothermic reaction. The energy stored in the chemical bonds of the products can be a form of renewable energy if solar energy is used in the photo-excitation [22]. This way we can simultaneously decrease the atmospheric CO_2 presence and exploit a renewable energy source.

The photocatalytic activity of titanium dioxide (TiO_2) has been a major topic of research due to its advantageous properties over other semiconductors: It is relatively cheap and readily available. It is chemically and biologically stable and possesses high oxidative potential. UV-irradiation generates electron–hole pairs in TiO_2 like in other semiconductors, which ends in powerful redox centers on the surface [23–29]. TiO_2 and its derivatives were reported in many papers as photocatalysts in the carbon-dioxide reduction [26–30]. However, the overall photocatalytic efficiency is consistently low hence further improvements are still required. A possible way to enhance the catalytic activity of a material is to increase its specific surface area. This research line in the case of TiO_2 was started in 1998: Kasuga et al. published the synthesis of a novel tubular shaped TiO_2 material with high specific surface area [8, 30–33].

The strenuous development of TiO_2 nanomaterials has thriven our knowledge with a new class of titania-based nanostructure, the layered titanate materials [8, 10, 32–35]. They are in the center of interest due to their extremely large ion-exchange capacity [8, 32, 34–39]. Their high surface area and cation exchange capacity ensure high metal dispersion (e.g. Ni, Co, Ag, Cu and Au) in/on their structure hence titanate nanostructures are promising supports for catalytic applications [40]. Titanate nanotubes (TNT) have got open ends. Their typical outer diameter is 7–10 nm and their length is generally 50–170 nm. Their cross section is spiral shaped and composed of 3–7 wall layers. The mean diameter of their inner channel is around 5 nm [8, 30, 41–43]. Their H-form ($H_2Ti_3O_7{\cdot}nH_2O$) contains physisorbed water on its surfaces, crystallographic water between their layers and –OH groups with ion exchangeable H^+ ions in their structure [44]. The curved layers consequently contains large amount of defect sites, typically oxygen vacancies and Ti^{3+} centers, which can make them promising photocatalysts, because the defect sites can trap photoelectrons or holes extending the lifetime of the excited state [8, 45]. The defect sites on their surfaces can stabilize considerably small sized metal clusters, too [38, 39]. From now on we denote $H_2Ti_3O_7{\cdot}nH_2O$ nanotubes as TNT in this paper.

The photocatalytic activity of N-doped ion-exchanged and modified TNT-s in several reactions was already investigated [29, 33]. Some activity in dye degradation, ethanol decomposition and CO_2 reduction was observed. Li et al. observed considerable activity in the CO_2+H_2O photoreaction in liquid phase with CdS modified TNT-s where methanol was accumulated in the reactor with approx. 45 μmol h^{-1} g^{-1} rate [46]. Ethanol was used during the synthesis of the catalysts, still the carbon source of methanol was not verified in this report. Parayil et al. investigated the CO_2+H_2O photocatalytic reaction in gas phase on C and N doped sodium-TNT [47]. They detected methane as the main product with 9.75 μmol h^{-1} g^{-1} formation rate but the reaction was followed only for 1 h in a static system. Most of the works investigate the photocatalytic activity of doped and modified titanates and are restricted to common dye degradation tests which tell us insufficient information on their functionality [48–50]. In order to understand how CO_2 can be photocatalytically reduced to methane, studying the mechanism of the backward reaction could be very useful, too. Very little attention was devoted in the literature to this topic up to now.

Not only semiconductors, but metals themselves can also be photo-excited. It has been shown that the photon-driven bond breaking and bond formation of the adsorbates may occur for many adsorbed molecules on metal surfaces, despite the strong quenching of electronically excited states [51–53]. In certain cases the rate of the photochemical process is commensurable with the electronic quenching on

metal surfaces. The cross section is rather low, it is in the range of 10^{-18}–10^{-20} cm^2. These photo-induced mechanisms are appropriately described with the model involving sub vacuum hot electrons or photoelectrons [53–55]. The photo efficiency of pure, unsupported metals is too low to justify photocatalytic applications.

The photochemical activity of semiconductors is appreciably enhanced by doping and metal nanoparticle depositing [24, 56]. The photocatalytic performance of a semiconductor is determined greatly by the rate of recombination of photo-excited electron–hole pairs (excitons). The nature of the dopants, impurities or defects in the crystal structure can have strong positive or negative effect on the recombination rates [45]. Generally, depositing noble metals onto the semiconductor surface can appreciably suppress the rate of the exciton recombination as they serve as electron sinks [57–61]. The mechanism of the electron trapping in n-type semiconductors such as TiO_2 is explained by the Schottky barrier which prevents the backward movement of electrons from the metal to the semiconductor [62]. Metals with large work functions such as Pt, Pd, Rh and Au are suitable to generate high energy Schottky barriers hence the electron–hole separation can be more effective [8, 24, 56]. An additional property of metal particles, the localized surface plasmonic resonance (LSPR), can play an important role in photocatalysis. It has been already investigated in the case of titanate or titania supported gold catalysts and it was suggested that the photo-excitation of LSPR can take part in the photochemical mechanisms [8, 33, 58, 61, 63–66].

Recently we studied the photo-induced reactions of methane on sodium-free (H-form) TNT doped with Rh and Au nanoparticles [61]. The pristine TNT was photocatalytically active in the CH_4–transformation reaction as well, but the addition of nanosized metal particles increased the formation rates significantly. It was also shown that the adsorption characteristic of gold strongly depends on the particle sizes. The electron transfer step can even occur on the surface of the gold particles due to the excitation of the local surface plasmon resonance or electron transitions in the molecular-like metal-adsorbate interactions. It was concluded that Rh initiates hydrogen formation while the gold nanoparticles more likely couples the methyl radicals. The activity of the Rh/TNT catalysts significantly decreased in irradiation time while the Au/TNT kept its activity. The activity decrease in the case of Rh/TNT was explained with the formation of structured surface carbon deposits. It was concluded that Rh can stabilize methine and methylene surface groups because it was prominently active in methane degradation [67, 68]. TNTs contain structural water and –OH groups basically that cannot be completely removed without permanent structural changes, thus H_2O/–OH is always present in the system [8, 38, 44]. In the elucidation of the mechanism of the methane transformation on Au and Rh modified TNTs it was strongly suspected that this crystallographic water or the surface OH-groups play an important role in the reaction. In addition, it was shown with electron paramagnetic resonance that the water and carbonates have got important roles in the overall photocatalytic reduction of carbon dioxide using TiO_2 [69]. Water plays an also important role in the photocatalytic H_2 production from ethanol–water mixtures over Pt/TiO_2 and Au/TiO_2 photocatalysts [70] and in alcohol-water mixtures on Au doped hydrogen TNT [10].

In order to prove the positive effect of water, in the present work we thoroughly investigated the photocatalytic CH_4+H_2O reaction on Au and Rh doped TNTs. The effect of CO_2 addition to the system was also studied. We chose anatase TiO_2 as reference catalyst instead of the more conventional P25 TiO_2 because the incidental structural changes in TNTs under mild conditions generally led to the formation of anatase phase [8, 33, 34]. First we characterized the catalysts with X-ray photoelectron spectroscopy (XPS) and high resolution transmission electron microscopy (HRTEM). Then we performed photocatalytic reactions using a quartz reactor in continuous flow mode. We followed the photo initiated reactions of CH_4+H_2O and CH_4+CO_2+H_2O system as well. The surface of the catalysts during the photoreactions was monitored using diffuse reflectance infrared spectroscopy (DRIFTS). Physicochemical characterization including XPS and temperature programmed reduction (TPR) of the used catalysts were also performed.

2 Materials and methods

2.1 Preparation and characterization of the catalysts

Based on the literature results [8, 33, 71, 72] the nanotubular structures could be obtained from different type of TiO_2 precursors (including anatase and rutile). In the present work Degussa P25 TiO_2; 80% rutile and 20% anatase (purity: 99.5%) was used. H-form TNT ($H_2Ti_3O_7{\cdot}nH_2O$) were synthesized by an alkali hydrothermal method described previously [8, 30, 32, 33, 38, 43, 61]. The as-synthesized TNT were analyzed with different methods including XPS, DTG-MS and DRIFTS. Hydrocarbon fragments were not detected, only adsorbed water and OH groups could be identified [38]. The gold nanoparticle decorated TNTs were synthesized with the sodium borohydride method [39, 61, 73]: 1 g nanotube was added to 100 ml distilled water and suspended by ultrasonication. Then 5.2 ml of $HAuCl_4$ solution was added to the nanotube suspension. The concentrations were calculated to provide 1 wt% gold at the end of the synthesis. After this $NaBH_4$ solution was added quickly to the suspension for rapid reduction of $AuCl_4^-$ anions to small sized metallic gold particles. The reducing solution was made of 50 mg

$NaBH_4$ dissolved in 5 ml distilled water. The suspension was kept stirred for an additional 20 min then filtered with a sintered glass filter (G4, 5–15 μm) and washed with distilled water. Then the sample was dried in an electric exsiccator at 350 K for 16 h. We tried to avoid the undesired phase transformation of TNT with this low-temperature method [39].

The Rh/TNT catalyst was synthesized by incipient wetness impregnating the TNT with $RhCl_3$ solution to yield 1 wt% metal content [32, 38]. The impregnated powder was dried for 3 h in air at 383 K. The catalyst got further pretreatment just before the photocatalytic measurements in order to form Rh^0 state: the sample was annealed in oxygen flow for 1 h at 473 K and then flushed with argon then reduced in hydrogen flow for 1 h at 523 K, finally flushed with argon for 1 h at 523 K. In contrast to the Au/TNT composite the nanotube phase is stable up to 573 K in Rh/TNT hence the applied temperatures are in the safe range [38].

Anatase TiO_2 (Hombikat UV-100; purity: 99.0%) powder was impregnated with $HAuCl_4$ solution using the same method as for Rh/TNT to get Au/TiO_2 with 1 wt% gold content. The preparation procedure was identical with Rh/TNT. The impregnation technique generally results in bigger sized nanoparticles than the reduction with $NaBH_4$. Comparing this catalyst with the Au/TNT sample we can investigate the effect of the gold particle size on the mechanism.

We avoided the use of carbon containing compounds during the preparations in order to prevent incidental carbon contamination. These kinds of carbon contaminations could result in misleading conversions and artifact products [27]. The photocatalytic activity of both the pure supports and the composites were investigated with exactly the same reaction parameters.

At least 99.9 vol% pure gases were used in the pretreatment and preparation processes. In some cases further purification was applied with an in-line adsorption trap to remove carbon-dioxide and water contaminations. Triply distilled water was used for the catalyst preparation. The purities of the materials used in the synthesis were 99.9, 99.99 and 98 mol% for $HAuCl_4{\cdot}nH_2O$, $RhCl_3{\cdot}3H_2O$ and $NaBH_4$, respectively.

A Belcat A instrument (MicrotracBEL Corp.) was used to measure the BET surface areas of the materials. The instrument uses a single point method. The measured surface areas are the following: 278, 330, 264, 268 and 310 $m^2\ g^{-1} \pm 10\%$ for TiO_2, TNT, Au/TiO_2, Rh/TNT and Au/TNT, respectively.

The morphology of Au/TNT and Au/TiO_2 catalysts was characterized by a FEI Tecnai G^2 20 X-Twin transmission electron microscope using 200 kV operation voltage, ×180,000 magnification and 125 pm/pixel resolution. The particle size distribution of the deposited metal was determined by image analysis of the HRTEM pictures using the ImageJ software. The diameter distribution histogram was constructed from at least 100 individual nanoparticle diameter measurements. Simple average calculation was applied in cases when not enough particles were detected.

XP spectra were collected with a SPECS instrument equipped with a PHOIBOS 150 MCD 9 analyzer, which was operated in the FAT mode with 20 eV pass energy. The Al Kα radiation ($h\nu = 1486.6$ eV) of a dual anode X-ray gun was used for excitation. The gun was operated at 210 W (14 kV, 15 mA) power. Five scans were summed to get a single high-resolution spectrum. The maximum of the Ti $2p_{3/2}$ peak (458.9 eV) was used as binding energy reference. Self-supporting pellets were used in the XPS measurements. SpecsLab2 and CasaXPS software packages were used for spectrum acquisition and evaluation.

The quantity and reactivity of the surface carbon deposits were analyzed with TPR method: The spent catalyst was placed into a 10 cm long quartz tube and heated up from room temperature to 1173 K linearly at 15 K min^{-1} rate in 40 ml min^{-1} hydrogen flow. The products were analyzed with gas chromatography (Agilent 7890, HP Carbonplot capillary column, FI and TC detectors).

2.2 Photocatalytic tests

A flow-type cylindrical photoreactor was used for the photocatalytic reactions. The structure of the reactor was described in detail previously [61]. A high pressure mercury-arc lamp (undoped TQ-718) operated at 500 W was used for irradiation. Typically 0.5 g catalyst was used in the reactions. The reactant gases were mixed by mass flow controllers: 0.9 $cm^3\ min^{-1}$ methane was introduced into 28.2 $cm^3\ min^{-1}$ argon then bubbled through water at 298 K at atmospheric pressure to get surplus 0.9 $cm^3\ min^{-1}$ water vapor stream and to finally produce 30 $cm^3\ min^{-1}$ CH_4–H_2O–Ar mixture (CH_4:H_2O = 1:1 molar ratio). For the other experiment 0.9 $cm^3\ min^{-1}$ CH_4 and 0.9 $cm^3\ min^{-1}$ CO_2 were introduced into 27.3 $cm^3\ min^{-1}$ argon then bubbled through 298 K water to get CH_4–CO_2–H_2O–Ar mixture with CH_4:CO_2:H_2O = 1:1:1 molar ratio. A blank experiment was also carried out where 29.1 $cm^3\ min^{-1}$ argon was bubbled through water at 298 K to get H_2O–Ar mixture. The average dwell time of the reactants was approximately 16 min considering the overall flow rate ($v = 30\ cm^3\ min^{-1}$) and the volume of the reactor (476 cm^3).

The products formed in the photoreactions were analyzed with a Hiden HPR-70 mass spectrometer equipped with an electron ionizer source, a HAL3F-RC quadrupole mass selector and an 8-way batch inlet sampling system. Chromatographic separation was not used. Samples were taken from the gas stream at the inlet and the outlet of the reactor during the experiments and the signal differences (signal at inlet subtracted from the signal at outlet) were used further in the evaluations. The signal intensity $\left(y_i(t)\right)$ at the 2, 15, 16, 18, 26, 27, 28, 29, 30, 31, 43, 44 and 45 m/z values ($y_i(t)$ refers

to the differential signal) were followed. The spectrometer was previously calibrated for all expected products.

The photocatalytic measurement sequence consisted of a 6 h baseline section and 18 h UV-section where the irradiation was periodically paused for 3 h in every 6 h. The catalyst temperature (T) was around 403 K during the irradiation due to the undesirable heat effect of the lamp. The catalyst was heated to 403 K in the dark sessions too, to minimize the temperature fluctuation. The following photocatalytic reactions were performed: the CH_4+H_2O reaction and the CH_4+CO_2+H_2O reaction. An additional blank experiment was also carried out with water–argon mixture. The blank experiment was applied to check the origin of the products. The registered $y_i(t)$ functions were transformed to $r_i(t)$ functions (formation rate) in μmol h^{-1} g^{-1} units according to Eq. (1) where f_i stands for the calibration factor (from signal to molar fraction) of the i-th component, v is the overall flow rate of reactants and m_{cat} means the mass of the used catalyst.

$$r_i(t) = f_i\, y_i(t)\, \frac{p\, v}{R\, T\, m_{cat}} \tag{1}$$

The mean formation rates of the 9 h irradiation $\left(\overline{r_i}\right)$ were calculated in μmol h^{-1} g^{-1} units for all the products and reactants according to Eq. (2).

$$\overline{r_i} = \frac{1}{9h} \int_{6h}^{24h} r_i(t)\, dt \tag{2}$$

The rates with negative sign correspond to the reactants.

Broadband apparent quantum yield (Z) was calculated in all experiments. First we measured the irradiance ($E_{\lambda 1-\lambda 2}$) at the distance of the catalyst with a thermal detector in the 200–350 nm and in the 350–2000 nm ranges. This gave 0.143 (± 16%) and 0.199 (± 6.5%) W cm^{-2} values [61]. Then we normalized the spectral power distribution (SPD) curve (M(λ)) of the lamp with the measured irradiance value according to Eq. (3).

$$E_{200-350} = \int_{200}^{350} M(\lambda)\, d\lambda \equiv 0.143\ \mathrm{Wcm^{-2}} \tag{3}$$

The normalized SPD curve (M'(λ)) was then converted to spectral photon flux (Φ(λ)) in mol h^{-1} cm^{-2} nm^{-1} units using the Avogadro constant (N_A) according to Eq. (4).

$$\Phi(\lambda) = \frac{M'(\lambda)\, \lambda}{h\, c\, N_A} \tag{4}$$

Then absolute incident photon flux was calculated for each catalyst according to Eq. (5) by integrating the spectral photon flux from 200 nm to the wavelength of the bandgap (E_g) which was determined previously [61].

$$\Phi_{200-E_g} = \int_{200}^{E_g} \Phi(\lambda)\, d\lambda \tag{5}$$

Finally the broadband apparent quantum yield referring to the formation of the main product (hydrogen) was calculated with Eq. (6) where A stands for the catalyst covered area (=430 cm^2).

$$Z_{H_2} = \frac{\overline{r_{H_2}}\, m_{cat}}{A\, \Phi_{200-E_g}} \tag{6}$$

This quantity represents UV-source specific data because a UV-source with multiline spectrum (a high pressure mercury arc lamp) was used for excitation. The AQY values should be determined at a discrete wavelength for better comparability hence care must be taken when comparing the actual Z_{H2} values with the more frequently used AQY values in the literature [74, 75]. Otherwise, for a precise real quantum yield determination we should use monochromatic light and should know the quantity of the absorbed photons instead of the incident photons [76, 77].

The surface of the catalysts was investigated in-situ by infrared spectroscopy. An Agilent Cary-670 FTIR spectrometer was used with Harrick Praying Mantis diffuse reflectance system. The sample holder had BaF_2 windows in the infrared beam path and an additional quartz window for UV-irradiation. A focused mercury lamp (Osram, HBO 100 W/2, short arc) was used for UV excitation. 16 scans were recorded at 2 cm^{-1} spectral resolution. The background was recorded just after the pretreatment. The applied temperatures and gases were the same as used in the photocatalytic experiments. The UV irradiation was paused when the spectra were collected. After 1 h irradiation the reactants were flushed out from the sample space with inert gas and a final spectrum was collected after 30 min flushing in all experiments.

3 Results and discussion

3.1 Characterization of the supported Rh and Au catalysts

Au/TNT was characterized in detail by XPS previously [39, 61]. Symmetric Au $4f_{5/2}$ and $4f_{7/2}$ emissions were observed at 87.7 and 84.0 eV which correspond to Au^0. An additional peak at 85.9 eV (Au $4f_{7/2}$) appeared, too. This peak at higher binding energies can be the result of core level shifts due to low particle size [39, 78]. Another possible explanation is that Au^{n+} ions may occupy some of the ion exchange positions of TNT [39]. The TEM image on Fig. 1 shows the tubular morphology of the TNT support and the arrangement of the Au nanoparticles on it.

The average diameter of the nanotube channels is 7 nm. Particle size distribution was calculated and plotted in Fig. 1. The size of the identified Au nanoparticles is in the 1–8 nm

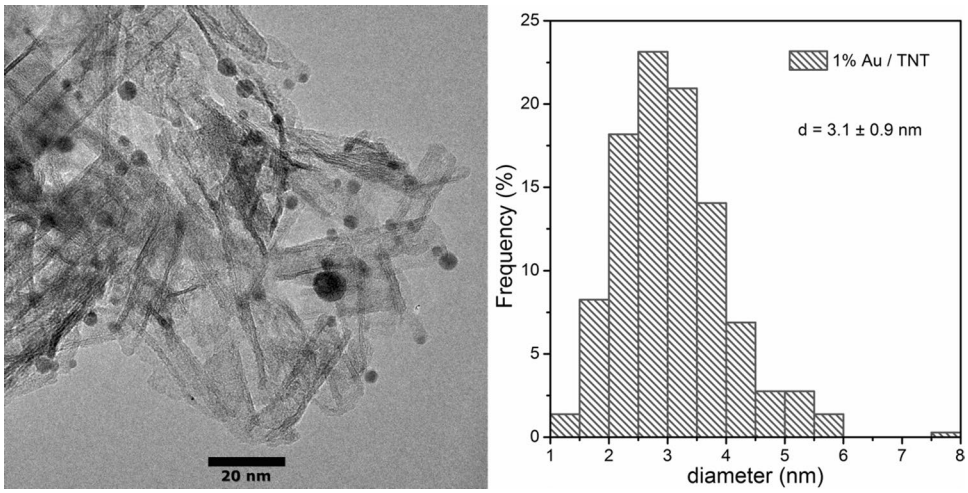

Fig. 1 TEM image (left) and the size distribution of Au particles (right) of Au/TNT

range. The average particle size is 3.1 ± 0.9 nm, and the most abundant size is 2.5–3.0 nm. Smaller than 1.5 nm sized particles were found, too, where the molecular-like behavior of gold becomes dominant [79, 80]. The UV–Visible absorption characteristics of Au/TNT was also studied previously with diffuse reflectance method: a strong absorption band at 2.31 eV (534 nm) appeared in the spectrum of Au/TNT which corresponds to the excitation of the local surface plasmon resonance of gold nanoparticles [61, 81]. We identified the absorption bands of the molecular-like transitions, too. UV absorptions were observed at 2.68, 2.93 and 3.19 eV [61]. Recently it was published that Au_{25} clusters exhibit multiple molecular-like transitions in its optical absorption spectrum: at least three well-defined bands at 1.8, 2.75 and 3.1 eV were observed in the UV–Vis spectrum [82].

XPS measurements of the pretreated Rh/TNT catalysts were performed recently [38]. The Rh $3d_{5/2}$ peak appeared at 309.3 eV in the case of 1% Rh content while at 308.3 eV on the catalyst with 2% Rh. These energies are higher than for Rh^0 (307.1 eV) which suggest an oxidized state of Rh. On the other hand very small Rh clusters can result higher binding energies, too. The average Rh particle size determined from TEM experiments resulted in 2.8 nm, but as small as 1 nm sized metal particles were detected, too [32, 38].

The pretreated Au/TiO_2 catalyst was investigated with TEM. The corresponding TEM image is shown in Fig. 2. The average particle size of Au was calculated from 13 diameter measurements and resulted in 7.4 ± 2.7 nm. This is in the range of the size of the support (Hombikat UV-100, anatase), and is significantly higher than in the case of Au/TNT (Fig. 1). According to XPS analysis, the Au $4f_{7/2}$ peak appeared at 84.0 eV (not shown). No high energy side shoulder was observed which could be attributed to very small clusters or positively charged Au. Due to the higher particle size of gold the relative contribution of the plasmonic character of it is pronounced [61]. The most important

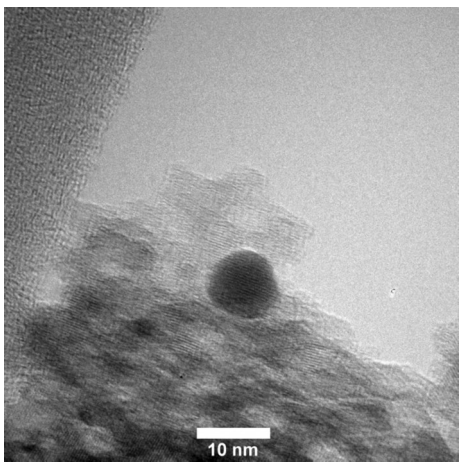

Fig. 2 TEM image of the Au/TiO_2 catalyst

parameters of the catalysts of the recent work are collected in Table 1.

3.2 Photocatalytic test experiments

The methane can be photo-converted on all catalysts as the photocatalytic tests showed. Figure 3 depicts the methane conversion and product formation as a function of irradiation time observed in the CH_4+H_2O reaction. The non-zero values in the initial molar fractions of the products are due to the residual gas background of these molecules. The molar fractions of the products are increases but the quantity of methane decreases in the UV periods as can be seen. Hydrogen, carbon dioxide and ethane were identified as main products. Higher methane consumption and hydrogen formation were observed on Rh/TNT comparing to Au/TiO_2 and Au/TNT, on the other hand decreasing molar fractions could be observed in this case. This drop

is assumed to be the result of activity loss because it is restricted to the UV active periods. In the case of Au/TNT and Au/TiO_2 no activity loss was observed in the experiments but also smaller methane conversions occurred. The Au/TiO_2 catalyst showed higher activity than the Au/TNT as demonstrated in Fig. 3. A small amount of methanol was also detected on all catalysts (not shown).

These catalysts showed the same behavior when carbon dioxide was introduced into the system as reactant (Fig. 4). The main products were hydrogen and ethane, and the same tendency was observed as in the CH_4+H_2O reaction: higher

Table 1 The most important parameters of the catalysts used in the present work

Catalyst	Rh/TNT	Au/TNT	Au/TiO_2
Support	$H_2Ti_3O_7{\cdot}nH_2O$ tube	$H_2Ti_3O_7{\cdot}nH_2O$ tube	TiO_2 anatase 10 nm
Impregnation	Incipient wetness	In suspension	Incipient wetness
Metal reduction	In situ, H_2	With $NaBH_4$ solution	In situ, H_2
Metal content (wt%)	1.0 ± 0.1	1.0 ± 0.5	1.0 ± 0.1
BET surface area ($m^2\ g^{-1}$)	268 ± 27	310 ± 31	264 ± 26
Average metal particle size (nm)	2.8 ± 0.7	3.1 ± 0.9	7.4 ± 2.7
Bandgap (eV) [61]	3.08	3.03	3.04

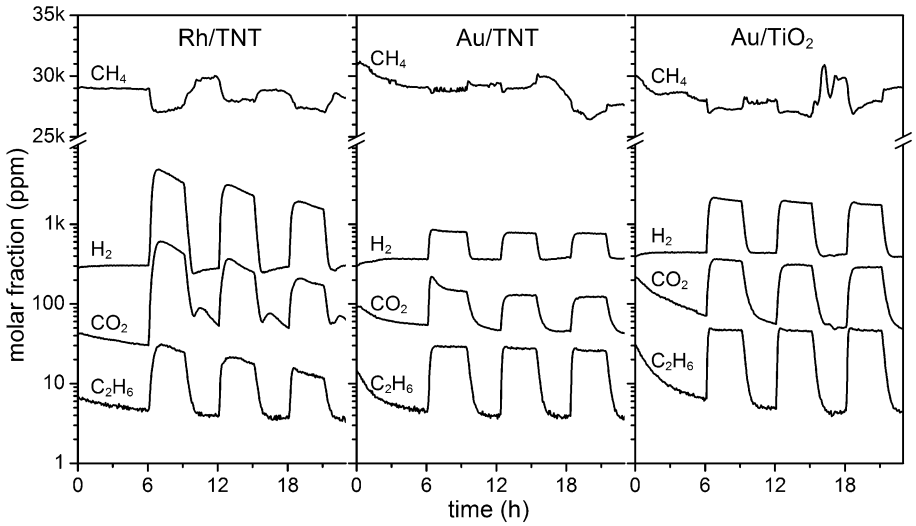

Fig. 3 The changes in the molar fractions in time on Rh/TNT, Au/TNT and Au/TiO_2 catalysts in the CH_4+H_2O reaction (the absolute signals at the reactor outlet after conversion to ppm are plotted)

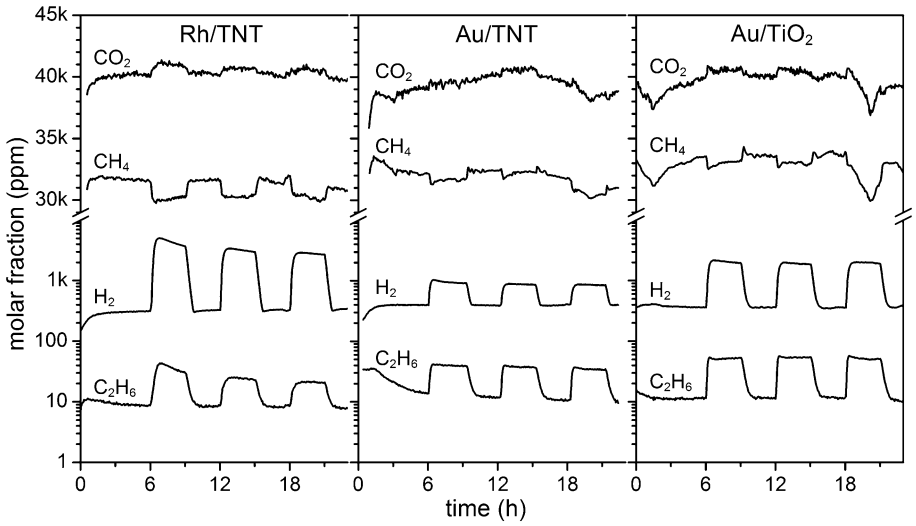

Fig. 4 The molar fraction changes of the analyzed molecules as a function of experiment time on Rh/TNT, Au/TNT and Au/TiO_2 catalysts in the CH_4+CO_2+H_2O reaction (The absolute signals at the reactor outlet after conversion to ppm are plotted)

methane consumption and hydrogen formation rates but activity loss occurred in the case of Rh/TNT. Carbon dioxide transformation was not observed, on the contrary, CO_2 formed as in the CH_4+H_2O reaction. Au/TiO_2 again showed higher activity than Au/TNT.

We calculated the formation rates of the various products for better comparison and to analyze the effect of CO_2 introduction. Table 2 shows the mean formation rates of the identified products. Methane conversion values (K_{CH4}) were calculated, too. We present in the table our earlier results on CH_4 decomposition, too, for easier comparison. The main products of the methane transformation are H_2 and ethane but some CO_2, CO and methanol also form. The accurate analysis of water consumption or formation was not feasible in our experiment setup. Carbon-dioxide can be a product or reactant, too. As can be seen the pure supports had the lowest activity in the methane conversion. The addition of metal significantly increased the rate of methane consumption in all reaction types.

Au/TNT and Rh/TNT showed the same activity in methane conversion when water was not present in the reactants. The methane conversion values were 1–2%. Au/TiO_2 was less active in these experiments (K_{CH4} < 1%). CO_2 and CO formed which is the consequence of an oxygen source. Some adsorbed water is always present and can act as an oxygen source as we pointed out previously [61]. The addition of CO_2 beside methane had negligible effect on the rates and on the methane conversion values [61]. One order of magnitude more ethane formed on Au/TNT than in the other cases when water was not used as reactant. It means that the oxidation of methane stops at the methyl stage more frequently on Au/TiO_2 in dry conditions.

The introduction of water as a reactant had notable effect on the product distribution. The conversion of methane was the highest on Rh/TNT and the lowest on Au/TNT among the supported metals. The formation of hydrogen followed the same tendency, but generally higher formation rates were observed than in the dry experiments. The methane conversion and the rate of hydrogen formation were the highest on Rh/TNT in the CH_4+CO_2+H_2O reaction.

Au/TiO_2 worked better in the methane conversion than Au/TNT when water was present. On the contrary, Au/TNT showed higher activity under dry conditions. The values of the methane consumptions were practically alternated between Au/TNT and Au/TiO_2 when water was introduced. The most ethane formed on TiO_2 and Au/TiO_2. The deposition of gold did not increase further the rate of ethane formation which means that the methyl coupling also happens on the surface of the TiO_2 under wet conditions. The introduction of CO_2 had a significant effect on the Rh/TNT system when water was present. The rates of the methane consumption and the hydrogen formation increased by approximately 50%. The conversion of CO_2 was under our detection limit except in two cases when CO_2 was formed in spite of its high initial concentration. Therefore CO_2 rather forms than consumes in the experiments.

In order to examine if there is a carbon source or sink in the system a carbon balance (Δ_C) was calculated from the

Table 2 The mean formation rates of the products ($\overline{r_i}$), the methane conversions (K_{CH4}), the carbon balances (Δ_C) and the broadband AQY values regarding to hydrogen formation (Z_{H2}) in the different experiments

Reactants	Catalyst	$\overline{r_i}$ (μmol h^{-1} g^{-1})						K_{CH4} (%)	Δ_C (μmol g^{-1})	Z_{H2}
		CH_4	C_2H_6	H_2	CO_2	CO	CH_3OH			
CH_4 [61]	TNT	−8.7[c]	1.2[a]	1.4[b]	3.0[a]	bdl	bdl	0.23[c]	bdl	1.1×10^{-6}
	Rh/TNT	−50[a]	1.9	115	11[a]	5.4[b]	0.14[c]	1.4	261[b]	9.4×10^{-5}
	Au/TNT	−70[b]	12	116	18[a]	11[a]	1.0[b]	1.6[b]	143[c]	7.2×10^{-5}
	Au/TiO_2	−22[c]	1.5	48	9.3[a]	1.7[b]	0.11[c]	0.82[c]	bdl	4.8×10^{-5}
CH_4 H_2O	TNT	bdl	3.0	11[a]	6.2[a]	4.1[b]	0.19[c]	bdl	bdl	9.4×10^{-6}
	TiO_2	−24[c]	5.6	3.8[b]	6.0[a]	4.0[b]	0.44[b]	0.74[c]	bdl	3.1×10^{-6}
	Rh/TNT	−108[a]	2.0[a]	296[a]	41[a]	13[a]	bdl	3.0[a]	457[c]	2.3×10^{-4}
	Au/TNT	−25[a]	3.3	56[a]	13[a]	3.1[b]	0.57[c]	0.65[b]	bdl	4.0×10^{-5}
	Au/TiO_2	−79[b]	5.8	191	36[a]	6.5[b]	0.40[c]	2.0[a]	222[c]	1.3×10^{-4}
CH_4 CO_2 H_2O	TNT	−16[a]	1.5	bdl	bdl	bdl	0.27[c]	0.66[a]	108[b]	–
	TiO_2	bdl	6.9	6.0[a]	bdl	4.1[c]	0.64[b]	bdl	bdl	3.9×10^{-6}
	Rh/TNT	−155[a]	2.8	446	128[b]	17[b]	0.21[c]	3.6[a]	bdl	2.9×10^{-4}
	Au/TNT	−29[c]	3.6	63[a]	bdl	3.5[c]	0.51[c]	0.79[c]	156[c]	4.6×10^{-5}
	Au/TiO_2	−61[a]	5.3	190	70[c]	4.9 [c]	0.36[c]	1.7[a]	bdl	1.4×10^{-4}
H_2O	Rh/TNT	bdl	bdl	bdl	0.34[c]	bdl	bdl	–	–	–

bdl below detection limit (The detection limit is unique for each case.)

[a]Estimated deviation is > 10% but ≤ 25%

[b]Estimated deviation is > 25% but ≤ 50%

[c]Estimated deviation is > 50% but < 100%

mean formation rates. The calculation was performed by Eq. (7) and the results are shown in Table 2.

$$\Delta_C = \left(-\overline{r_{CH_4}} - 2\overline{r_{C_2H_6}} - \overline{r_{CO_2}} - \overline{r_{CO}} - \overline{r_{CH_3OH}}\right) \times 9h \quad (7)$$

In most of the cases the final error of Δ_C is more than 100% (marked with "bdl" in Table 2) due to the error propagation. The detection limit fluctuates between 50 and 800 µmol g^{-1}. The carbon balance is negative in some cases because some carbon is missing from the product stream and remained on the surface. The highest amount of surface carbon was about 3.7% respect to converted methane. The reason of the carbon sink can be some kind of carbon deposit or an undetected product. In most of the cases the experiments on Rh/TNT resulted in large Δ_C values.

An additional blank experiment was performed in order to exclude that the products do not originates from surface contaminations: the experiment with water-argon mixture did not result in hydrogen, methane or ethane formation. Only a trace amount of CO_2 evolved. This means that the products generally originate from the reactants. In short, the introduction of water increased the degree of methane conversion and hydrogen production in the methane decomposition reaction on Rh/TNT and on Au/TiO_2. This effect was more pronounced when CO_2 was also present as reactant.

The broadband AQY values regarding hydrogen formation (Z_{H2}) presented in Table 2 are quite low comparing to the AQY percentages reported in water splitting reactions (these are very often above 50%) [74]. Some high quantum yield values were reported in the CO_2 photoreduction, too, but these values are not comparable directly with ours because the absorbed fraction of the incident photons is unknown in our case [26]. The difference between the values within the column follows exactly the tendency of the hydrogen formation rates because of the similar bandgap values. The reason of the low yields could be studied by investigating the efficiency of the consecutive steps of the mechanism [74]. This requires different methods and the exact knowledge of the reaction mechanism.

3.3 In-situ FTIR measurements

The infrared spectra collected after 1 h irradiation in the CH_4+H_2O and CH_4+CO_2+H_2O reactions are shown in Fig. 5. The pretreatment of the catalysts were carried out in situ in DRIFTS cell [61]. Some peaks appeared due to the adsorption of the reactants. No effect of the irradiation on the spectra was observed in these two reaction types. The adsorption of water resulted in the appearance of a broad band between 2700 and 3700 cm^{-1} (H-bridged stretching), negative peaks were detected at 3731 and 3660 cm^{-1} (ν_{as} and ν_s of H_2O), and absorptions around 1640 cm^{-1} ($\beta(H_2O)$). The evolution of the negative peaks means that the quantity of the isolated water molecules decreases as its surface concentration increases and H-bridged structure forms. The bending mode of two types of adsorbed water was observed at 1654 and 1632 cm^{-1} on the Rh/TNT and TNT catalysts. The $\beta(H_2O)$ vibration appeared at 1642 cm^{-1} in the case of Au/TNT. The adsorption of CO_2 ended up in small peaks at 1563 and 1382 cm^{-1} which are identified as surface bonded bidentate carbonates of the TNTs [83, 84]. The spectral absorptions of these surface carbonates were much stronger in the case of Rh/TNT when water was not applied as can be seen in Fig. 5. It means that water chemisorbs stronger than

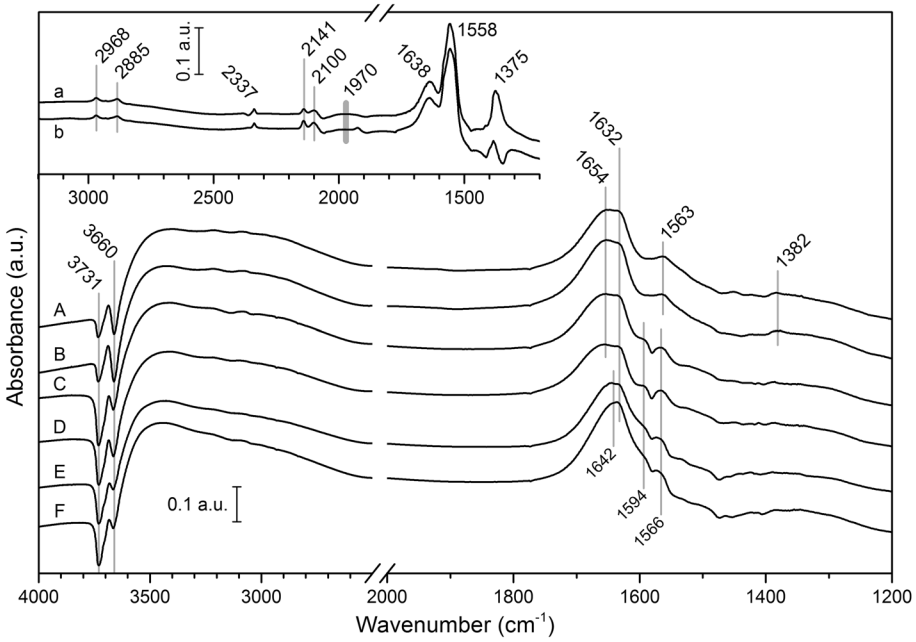

Fig. 5 In-situ DRIFT spectra collected after 1 h UV irradiation: CO_2+CH_4+H_2O reaction on Rh/TNT (*A*), on TNT (*C*) and on Au/TNT (*E*); CH_4+H_2O reaction on Rh/TNT (*B*), on TNT (*D*) and on Au/TNT (*F*); CO_2+CH_4 reaction on Rh/TNT (*a*) [61], CH_4 decomposition on Rh/TNT (*b*) [61]. The sample space was flushed with helium

CO_2 on the surface of TNTs. The appearance of the band as a shoulder at 1594 cm^{-1} may indicate that formate can also form during the adsorption of the reactants when Rh is not present [83, 84]. This formate can act as an intermediate which easily transforms to carbonate and probably to methanol in the presence of water [85, 86].

Bands were observed in the range of 1800–3000 cm^{-1} in the case of Rh/TNT when water was not present as reactant (inset in Fig. 5). These peaks appeared under irradiation and it was concluded previously that some of these features are due to important changes occurred on the catalyst surface (surface carbonaceous deposits and the re-oxidation of Rh particles) [61]. The lack of these peaks under wet conditions means that water just blocks these adsorption sites of CO and CO_2 but not prevents the formation of surface deposits and the oxidation of Rh.

3.4 Study of spent catalysts

XPS measurements were made on the spent catalysts in the binding energy range of O 1s and C 1s orbitals from the Rh/TNT and Au/TiO_2 catalysts used in the CH_4+CO_2+H_2O reaction (Fig. 6). The used catalyst was placed in the preparation chamber connected to the main analysis chamber. After flashing with argon, the sample was introduced to the vacuum chamber (10^{-8} mbar) for XPS analysis [61].

The lattice oxygen of TiO_2 is represented by the 530.8 eV O 1s peak (Fig. 6a) [38, 87]. The photoemission peak at 532.7 eV involves single fold oxygen or –OH species [38], oxygens of organic C=O or C–O–R bonds [88] and organic carbonate species [89]. The peak at 528.5 eV could not be clearly identified. We could resolve the C 1s region into four peaks (Fig. 6b): The peak at 289.9 eV corresponds to carbonate ions [87]. C–O–C carbon was detected at 287.5 eV [90]. Carbon with sp^3 hybrid state (i.e. C, CH, CH_2 or CH_3) can be identified at 285.4 eV [88, 90]. Carbidic carbon at 282.2 eV was also identified [87]. C^0 with sp^2 hybrid state in the range of 284–285 eV was not detected [88, 90].

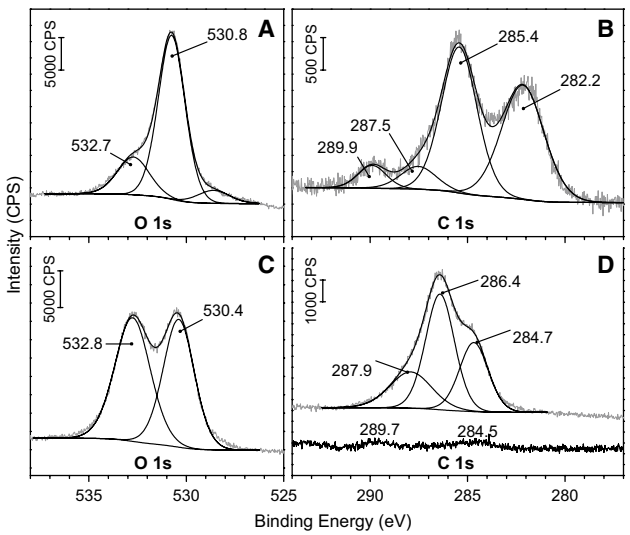

Fig. 6 The O 1s and C 1s XP spectra of Au/TiO_2 (anatase) (**a** and **b**) and Rh/TNT (**c** and **d**) catalysts used in the CH_4+CO_2+H_2O reaction. Additional C 1s spectrum (lower) shows the carbon region before use, just after reduction (**d**)

Figure 6c shows the O 1s XP spectra of the Rh/TNT catalyst spent in the CH_4+CO_2+H_2O reaction. The lattice oxygen of TNT appeared at 530.4 eV (O 1s). The peak at 532.8 eV represents mainly –OH species which have got greater number in TNT comparing to TiO_2 according to the peak areas [38]. This is in accordance with the main structural differences as TNT contains larger amount of ion exchangeable –OH groups than TiO_2 [8, 44]. However the peak at 532.8 eV can also involve organic C=O and C–O–R oxygens [88]. The carbon 1s region could be deconvolved into three peaks (Fig. 6d): The peak at 284.7 eV corresponds to C^0 with sp^2 hybrid state [88, 90]. The peak at 286.4 eV is characteristic for the C–OH carbons [88]. The binding energy at 287.9 eV corresponds to C=O carbon which can originate from the Rh-chemisorbed carbon-monoxide molecules [90]. Carbonates and carbidic carbons were not clearly resolved in this sample. Additional C 1s spectrum (lower) shows the carbon region before use, just after reduction (Fig. 6d). The observed intensity of this background is significantly lower than that was detected after reaction. This gives a strong proof that the detected carbon signals originate from the reaction.

It can be assumed from the activity loss and from the XPS results that surface carbon forms during the reactions especially on the Rh/TNT catalyst. In order to measure the quantity and reactivity of this surface deposit TPR experiments were carried out. In TPR experiments we measured only Rh/TNT catalysts used in the different reactions. Two blank experiments were performed which confirmed that the pre-treated sample is free of reducible surface carbon and the thermal decomposition of methane is negligible. The formation of methane was detected on spent Rh/TNT catalyst. The methane formation rate is plotted in Fig. 7 along with our earlier measurements on Rh/TNT obtained in similar way for easier comparison [61]. Small amount of ethane and carbon-dioxide also formed in these experiments. The detected methane and ethane means that the surface contains easily reducible carbonaceous deposits which formed under irradiation. The carbon dioxide originates from surface carbonates which simply desorbs at elevated temperatures.

The formation rate of methane have got a maximum which is around 650 K in all cases. Additionally, a higher temperature peak can be observed around 900 K in the experiments where water was a reactant, too. This means that the structure of the carbonaceous deposits slightly differs under dry and wet conditions. XPS experiments

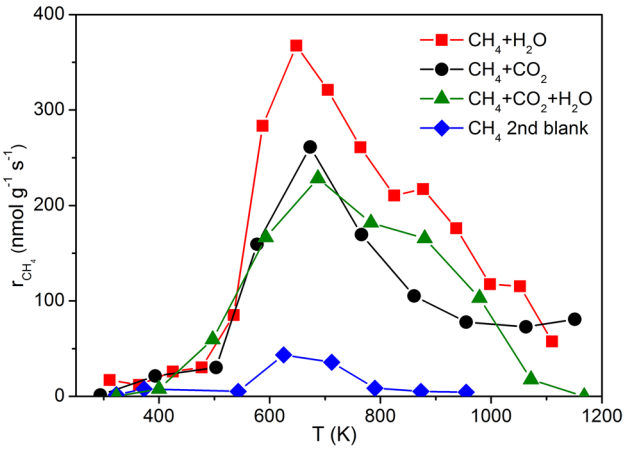

Fig. 7 The methane formation rates during the TPR measurements of the spent Rh/TNT, catalyst. The curves with filled square and filled circle symbols are from our previous work [61]. Blank experiment performed on pretreated catalyst is also shown

showed several oxidized forms of surface carbon in the CH_4+CO_2+H_2O reaction (Fig. 6d), more than in our previous studies on CH_4 transformation [61]. The higher temperature TPR peak can represent the reduction of C=O carbon detected at 287.9 eV in XP spectra.

The overall quantity of methane formed related to catalyst unit mass in the TPR experiments was calculated by the time integral of the TPR curves. The values are 528, 354 and 384 μmol g^{-1} in the CH_4+H_2O, CH_4+CO_2 and CH_4+CO_2+H_2O reactions, respectively. These results are in acceptable accordance with the Δ_C values presented in Table 2 except in the case of the CH_4+CO_2+H_2O reaction. The deviation is not understood yet. Generally 20–30 μmol g^{-1} methane formed in the TPR measurements made on the used Au/TNT and Au/TiO_2 catalysts. So the detected easily reducible carbon containing surface deposits are the byproducts of the photoreactions and formed in larger quantities on Rh catalysts.

3.5 Presumed photocatalytic mechanism for Rh catalysts

It turned out in our photocatalytic experiments that the titanate (in nanotube form) and titania nanostructures are active in methane transformation. The photochemical activity of titanate and titania is appreciably enhanced by Au and Rh nanoparticle deposition. As we already mentioned in the introduction, depositing metal onto the semiconductor surface can considerably suppress the rate of exciton recombination [24, 57, 60]. Dispersed Au and Rh crystallites serve as electron sinks in our case hence the increase in activity was expected. In case of gold nanoparticles the LSPR and the short-range (molecular-like Au clusters) interaction may play an important role in photocatalysis [58, 61, 63–65, 91]. Gold clusters is small size (d < 3 nm) lose their bulk-like electronic properties; for example, they no longer show the plasmonic excitation character [82].

We offer different mechanisms for Au and Rh catalysts because the adsorption characteristics of these metals are distinct. The activity of Rh/TNT towards methane conversion is better when water is present in the system and the best when CO_2 and H_2O are both introduced as reactants besides methane (Table 2). The surface composition of the catalyst is quite different in the presence of water than without it as can be seen from the DRIFTS results (Fig. 5). Only minimal amount of surface carbonate was detected besides adsorbed water under wet conditions unlike in the dry experiments where more carbonate appeared. In addition Rh-bonded CO and surface –CH_3 groups were also detected in the latter case. This means that water dominates the surfaces of both the support and the metal particles under wet conditions.

The rate of methane conversion and hydrogen formation slightly decreased over time on Rh/TNT catalyst (see Figs. 3, 4) because surface carbon deposits form in the reaction. The reactivity of the surface carbon is independent of the reaction type (Fig. 7). It contains mainly C–OR, additionally C^0 (with sp^3 hybrid state) and C=O carbons in the case of the CH_4+CO_2+H_2O reaction (Fig. 6). M–C carbons were not clearly resolved in this sample. So oxidized carbon deposits develop in the presence of water (C^0–C^{2+} carbons), but the surface deposit consisted mainly of C^0 (with more sp^2 character), additionally M–C and C–OR carbons under dry conditions [61]. Rh is more able than Au to dissociate CH_4 and –CH_x groups to hydrogen and surface carbon. The slight thermal decomposition of methane proceeds even on 423 K on Rh catalysts [16]. This is in accordance with our previous TPR results which suggest that methane slightly decomposes at 403 K on Rh/TNT [61].

Water must have an important role in the mechanism because of its promoting effect. It is generally accepted that water adsorbed on the surface of titanates or TiO_2 can prevent the electron–hole pair recombination by capturing the charges [71, 92]. The photogenerated holes can react with the adsorbed water resulting in OH radical and H^+. These species can delocalize on the surrounding H_2O (Eq. 8).

$$\mathrm{TNT}\left(h^+\right) + \mathrm{H_2O_{(TNT)}} \rightarrow \mathrm{TNT} + \mathrm{OH^*_{(TNT)}} + \mathrm{H^+_{(H_2O)}} \quad (8)$$

The electrons can be trapped by the proton formed as in (8) across the adsorbed water (9). The source of this electron can be the TNT support or the metal particle.

$$\mathrm{TNT}(e^-)/\mathrm{M}(e^-) + \mathrm{H^+_{(H_2O)}} \rightarrow \mathrm{TNT/M} + \mathrm{H^*_{(H_2O)}}/\mathrm{H^*_{(M)}} \quad (9)$$

Methane reacts with the OH radicals (10) then continues the oxidation to C^0 on the surface of Rh (Eq. 11). It

is generally accepted that the dehydrogenation process of methyl groups rather occurs on rhodium [93]:

$$OH^*_{(TNT)} + CH_{4(g)} \xrightarrow{M} H_2O_{(TNT)} + CH^*_{3(M)} \quad (10)$$

$$CH^*_{3(M)} \xrightarrow{M} CH^*_{2(M)} + H^*_{(M)} \rightarrow\rightarrow C_{(M)} + \frac{3}{2}H_{2(g)} \quad (11)$$

The hydrogen radicals which are the results of electron trapping or methane oxidation recombine to molecular hydrogen on the Rh surface (12). The hydrogen and methyl radicals can also recombine and produce methane (13).

$$2H^*_{(M)} \xrightarrow{M} H_{2(M)} \rightarrow H_{2(g)} \quad (12)$$

$$CH^*_{3(M)} + H^*_{(M)} \xrightarrow{M} CH_{4(M)} \rightarrow CH_{4(g)} \quad (13)$$

The conversion of CO_2 was not observed at all in the experiments but it had a promoting effect in one case: this effect was observed only when water was present and CO_2 must be in dissolved form. Dissolved CO_2 in carbonate form can act as hole scavenger, hence can elongate the lifetime of the electron–hole pairs (14) [69]. Additionally, hydrogen carbonates trapped by a hole can generate OH radicals, too (15) which can be responsible for the increased activity.

$$TNT\left(h^+\right) + CO^{2-}_{3(aq)} \rightarrow TNT + CO^{*-}_{3(aq)} \quad (14)$$

$$TNT\left(h^+\right) + HCO^{-}_{3(aq)} \rightarrow TNT + CO_{2(aq)} + OH^*_{(aq)} \quad (15)$$

3.6 Presumed photocatalytic mechanism for Au catalysts

We achieved higher methane conversions with Au/TNT under dry conditions than under wet conditions. The performance of the Au/TiO_2 catalyst was exactly the opposite. It operated better when water was a reactant, too. Additionally, more hydrogen formed in this case under wet conditions than with Au/TNT under dry conditions. Au/TNT and Au/TiO_2 differ not only in the support but also in their method of synthesis. The $NaBH_4$ reduced Au/TNT contains smaller Au particles while the average Au particle size in Au/TiO_2 is its double (Table 1). Both catalysts have gold particles with plasmonic or molecular like characters, too, as it was shown previously, but Au/TNT contains more molecular-like Au clusters [61]. Recently it was shown that this type of Au cluster sufficiently catalysis certain reaction; for example it can activate the CO in CO oxidation [94, 95]. We suggest that the molecular-like Au cluster may facilitate the activation of methane for transformation to dehydrogenation (13) and the coupling of methyl to ethane (16) which dominates on Au/TNT as can be seen in Table 2. It is generally accepted that the coupling of methyl radicals favored on gold [96]:

$$2CH^*_3 \xrightarrow{M} C_2H_6 \rightarrow C_2H_{6(g)} \quad (16)$$

Excess water blocks this mechanism probably at the stage of methane chemisorption hence the lower methane conversions. The scene of methyl coupling is relocated to the surface of the TNT or TiO_2 when water is present in excess because the presence of metal had no effect on the formation rate of ethane. The gold particles in Au/TiO_2 are mainly plasmonic. This catalyst may operates better when water is present probably due to the plasmon assisted dissociation of water which produces OH radicals on the surface. The as generated OH* can react with methane in a radical type reaction. This mechanism is not blocked but enhanced by water implicitly.

Only a small amount of surface carbonaceous deposit was formed in these reactions comparing to the Rh/TNT catalyst as can be seen from the TPR measurements (Fig. 7) and in the XPS measurements (Fig. 6). The surface carbon found on Au/TiO_2 is more oxidized than on Rh/TNT which can be the result of the more oxidative environment. No effect was observed on gold catalysts when CO_2 was introduced as reactant.

The formation of methanol was also detected in all experiments. The formation rates of methanol and ethane shows strong correlation (Table 2). This means that the formation of methanol (18) is a general side reaction of methyl coupling (16). CH_3–OH may also coupling but it is very likely that methyl groups reacts with lattice oxygen of oxide support, the formed methoxy species (which could be an intermediates in several catalytic processes [97]) reacts with hydrogen atoms:

$$CH^*_3 + O \rightarrow CH_3O \quad (17)$$

$$CH_3O + H \rightarrow CH_3OH \quad (18)$$

The rate of the further reaction of methyl radical determines the ratio of different products.

4 Conclusions

In the present study we confirm the role of structural H_2O/–OH of TNT in photocatalysis. For this purpose we investigated the photocatalytic conversion of methane with additional water.

It was demonstrated that methane can be photocatalytically transformed to hydrogen with relatively large cross section. The presence of water and CO_2 catalyzes this reaction. The route of the transformation is strongly determined by

the nature of the metal (Rh and Au) deposited on the TNT support. The size of the gold nanoparticles also affects the fundamental mechanism.

Hydrogen carbonates and surface water play key role in the methane transformation on Rh/TNT by capturing the photogenerated holes. This results in OH radical formation which can initialize the oxidation of methane. Metallic Rh accepts hydrogen from the methane degradation and recombines it as molecular hydrogen. In consequence a large amount of hydrogen and surface carbonaceous deposit forms in these reactions. The surface deposit occupies the surface of the catalyst and results in decreasing activity in time.

The plasmonic and molecular-like behavior of gold nanoparticles determine the reaction route of gold catalysts. The Au/TNT sample consisted of smaller nanoparticles which can capture the photogenerated electrons and activate the adsorbed methane in a molecular-like Au nanocluster–methane interaction. The formation of ethane was the most intensive in this case. The addition of water blocks this mechanism. The Au/TiO_2 catalyst with larger nanoparticles operates better in methane transformation under wet conditions. Its reason can be the more favored electron excitation of gold which results in activated water molecules on the metal surface. The environment on the surface of the catalyst is more oxidative, hence oxidized and less carbonaceous deposit forms than on Rh/TNT.

Acknowledgements The authors wish to thank *Erika Varga* for the XPS measurements, *Zsuzsa Ferencz* for the TPR measurements, *László Nagy* for the synthesis of the titanate nanotubes and *Tamás Varga* for the HRTEM measurements. Financial support of this work by the *National Research Development and Innovation Office* through grants *GINOP-2.3.2-15-2016-00013* and *NKFIH OTKA K120115* is gratefully acknowledged.

References

1. Lewis NS, Nocera DG (2006) Proc Natl Acad Sci 103:15729–15735
2. Lior N (2008) Energy 33:842–857
3. Fujishima A, Honda K (1972) Nature 238:37–38
4. Yu J, Zhang L, Cheng B, Su Y (2007) J Phys Chem C 111:10582–10589
5. Galindo C, Jacques P, Kalt A (2000) J Photochem Photobiol A 130:35–47
6. Yu J, Zhang J (2010) Dalton Trans 39:5860–5867
7. Kumar SG, Devi LG (2011) J Phys Chem A 115:13211–13241
8. Kukovecz Á, Kordás K, Kiss J, Kónya Z (2016) Surf Sci Rep 71:473–546
9. Kudo A, Miseki Y (2009) Chem Soc Rev 38:253–278
10. Dosado AG, Chen W-T, Chan A, Sun-Waterhouse D, Waterhouse GIN (2015) J Catal 330:238–254
11. Haryanto A, Fernando S, Murali N, Adhikari S (2005) Energy Fuels 19:2098–2106
12. Armaroli N, Balzani V (2011) ChemSusChem 4:21–36
13. Tahir M, Amin NS (2013) Renew Sustain Energy Rev 25:560–579
14. Edwards JH, Maitra AM (1995) Fuel Process Technol 42:269–289
15. Bradford MCJ, Vannice MA (1999) Catal Rev 41:1–42
16. Erdőhelyi A, Cserényi J, Solymosi F (1993) J Catal 141:287–299
17. Zhang Z, Tsipouriari VA, Efstathiou AM, Verykios XE (1996) J Catal 158:51–63
18. Sarusi I, Fodor K, Baán K, Oszkó A, Pótári G, Erdőhelyi A (2011) Catal Today 171:132–139
19. Papadopoulou C, Matrials H, Verykios XE (2012) In: Guczi L, Erdőhelyi A (eds) Catalysis for alternative energy generation, 1st edn. Springer, New York
20. Ferencz Z, Baán K, Oszkó A, Kónya Z, Kecskés T, Erdőhelyi A (2014) Catal Today 228:123–130
21. Yuliati L, Itoh H, Yoshida H (2008) Chem Phys Lett 452:178–182
22. Narayanan H, Viswanathan B, Yesodharan S (2016) Curr Catal 5:79–107
23. Henderson MA (2012) Surf Sci Rep 66:185–297
24. Ola O, Maroto-Valer MM (2015) J Photochem Photobiol C 24:16–42
25. Lan Y, Lu Y, Ren Z (2013) Nano Energy 2:1031–1045
26. Habisreutinger SN, Schmidt-Mende L, Stolarczyk JK (2013) Angew Chem Int Ed 52:7372–7408
27. Izumi Y (2013) Coord Chem Rev 257:171–186
28. Halasi G, Gazsi A, Bánsági T, Solymosi F (2015) Appl Catal A 506:85–90
29. Tahir M, Amin NS (2013) Energy Convers Manag 76:194–214
30. Kasuga T, Hiramatsu M, Hoson A, Seiko T, Niihara K (1998) Langmuir 14:3160–3163
31. Lee K, Mazare A, Schmuki P (2014) Chem Rev 114:9385–9454
32. Kukovecz Á, Pótári G, Oszkó A, Kónya Z, Erdőhelyi A, Kiss J (2011) Surf Sci 605:1048–1055
33. Bavykin DV, Friedrich JM, Walsh FC (2006) Adv Mater 18:2807–2824
34. Sun X, Li Y (2003) Chem—Eur J 9:2229–2238
35. Tsubota S, Haruta M, Kobayashi T, Ueda A, Nakahara A (1991) In: Poncelet G et al (eds) Preparation of catalysts V, 1st edn. Elsevier, Amsterdam
36. Cesano F, Bertarione S, Uddin MJ, Agostini G, Scarano D, Zeccina A (2010) J Phys Chem C 114:169–178
37. Madarász D, Pótári G, Sápi A, László B, Csudai C, Oszkó A, Kukovecz Á, Erdőhelyi A, Kónya Z, Kiss J (2013) Phys Chem Chem Phys 15:15917–15925
38. Pótári G, Madarász D, Nagy L, László B, Sápi A, Oszkó A, Kukovecz Á, Erdőhelyi A, Kónya Z, Kiss J (2013) Langmuir 29:3061–3072
39. Pusztai P, Puskás R, Varga E, Erdőhelyi A, Kukovecz Á, Kónya Z, Kiss J (2014) Phys Chem Chem Phys 16:26786–26797
40. Haspel H, Laufer N, Bugris V, Ambrus R, Szabó-Révész P, Kukovecz Á (2012) J Phys Chem C 16:18999–19009
41. Kordás K, Mohl M, Kónya Z, Kukovecz Á (2015) Transl Mater Res 2:015003
42. Zhang Y, Jiang Z, Huang J, Lim LY, Li W, Deng J, Gong D, Tang Y, Lai Y, Chen Z (2015) RSC Adv 5:79479–79510
43. Horváth E, Kukovecz Á, Kónya Z, Kiricsi I (2007) Chem Mater 19:927–931
44. Bavykin DV, Carravetta M, Kulak AN, Walsh FC (2010) Chem Mat 22:2458–2465
45. Linsebigler AL, Lu G, Yates JT Jr (1995) Chem Rev 95:735–758
46. Li X, Liu H, Luo D, Li J, Huang Y, Li H, Fang Y, Xu Y, Zhu L (2012) Chem Eng J 180:151–158
47. Parayil SK, Razzaq A, Park S-M, Kim HR, Grimes CA, In S-I (2015) Appl Catal A 498:205–213
48. Qamar M, Kim SJ, Ganguli AK (2009) Nanotechnology 20:455703
49. Peng S, Zeng X, Li Y (2015) Int J Hydrog Energy 40:6038–6049
50. Zhao X, Cai Z, Wang T, O'Reilly SE, Liu W, Zhao D (2016) Appl Catal B 187:134–143
51. Avouris P, Person BNJ (1984) J Phys Chem 88:837–848

52. Ying ZC, Ho W (1991) J Chem Phys 94:5701
53. Zhou X-L, Zhu X-Y, White JM (1991) Surf Sci Rep 13:73–220
54. Kiss J, Lennon D, Jo SK, White JM (1991) J Phys Chem 95:8054–8059
55. Jo SK, Zhu X-Y, Lennon D, White JM (1991) Surf Sci 241:231–243
56. Wu M-C et al (2011) ACS Nano 5:5025–5030
57. Subramanian V, Wolf EE, Kamat PV (2004) J Am Chem Soc 126:4943–4950
58. Jacob M, Levanon H, Kamat PV (2003) Nano Lett 3:353–358
59. Carp O, Huisman CL, Reller A (2004) Prog Solid State Chem 32:33–177
60. Bowker M, Morton C, Bahruj H, Greves J, Jones W, Davis PR, Brookes C, Wells PP, Dimitratos N (2014) J Catal 310:10–15
61. László B, Baán K, Varga E, Oszkó A, Erdőhelyi A, Kónya Z, Kiss J (2016) Appl Catal B 199:473–483
62. Ioannides T, Verykios XE (1996) J Catal 161:560–569
63. Zhang N, Liu S, Fu X, Xu Y-J (2011) J Phys Chem C 115:9136–9145
64. Kowalska E, Mahaney OOP, Abe R, Ohtani B (2010) Phys Chem Chem Phys 12:2344–2355
65. Park H, Park Y, Kim W, Choi W (2013) J Photochem Photobiol C 15:1–29
66. Rycenga M, Cobley CM, Zeng J, Li W, Moran CH, Zhang Q, Qin D, Xia Y (2011) Chem Rev 111:3669–3712
67. Kiss J, Kis A, Solymosi F (2000) Surf Sci 454:273–279
68. Kecskés T, Barthos R, Raskó J, Kiss J (2003) Vacuum 71:107–111
69. Dimitrijevic NM, Vijayan BK, Pouektov OG, Rajh T, Gray KA, He H, Zapol P (2011) J Am Chem Soc 133:3964–3971
70. Jovic V, Al-Azri ZHN, Chen W-T, Sun-Waterhouse D, Idriss H, Waterhouse GIN (2013) Top Catal 56:1139–1151
71. Ying L, Gao X, Zhu H, Zheng Z, Yan T, Wu F, Ringer SP, Song D (2005) Adv Funct Mater 15:1310–1318
72. Hernandez-Alonso MD, Gracia-Rodriguez S, Sánchez B, Coronado JM (2011) Nanoscale 3:2233–2240
73. Bavykin DV, Lapkin AA, Plucinski PK, Torrente-Murciano L, Friedrich JM, Walsh FC (2006) Top Catal 39:151–160
74. Li X, Yu J, Low J, Fang Y, Xiao J, Chen X (2015) J Mater Chem A 3:2485–2534
75. Hisatomi T, Takanabe K, Domen K (2015) Catal Lett 145:95–108
76. Kisch H (2010) Angew Chem Int Ed 49:9588–9589
77. Serpone N (1997) J Photochem Photobiol A 104:1–12
78. Henry CR (1998) Surf Sci Rep 31:231–325
79. Sasahara A, Pang CL, Onishi H (2006) J Phys Chem B 110:17584–17588
80. Kelly KL, Coronado E, Zhao LL, Schatz GC (2003) J Phys Chem B 107:668–677
81. Chandrasekharan N, Kamat PV (2000) J Phys Chem B 104:10851–10857
82. Zhu M, Aikens CM, Hollander FJ, Schatz GC, Jin R (2008) J Am Chem Soc 130:5883–5885
83. Baltrusaitis J, Schuttlefield J, Zeitler E, Grassian VH (2011) Chem Eng J 170:471–481
84. Collins SE, Baltanás ME, Bonivardi AL (2004) J Catal 226:410–421
85. Dobson KD, McQuillan AJ (1999) Spectrochim Acta Part A 55:1395–1405
86. Tóth M, Varga E, Oszkó A, Baán K, Kiss J, Erdőhelyi A (2016) J Mol Catal A 411:377–387
87. Dupin J-C, Gonbeau D, Vinatier P, Levasseur A (2000) Phys Chem Chem Phys 2:1319–1324
88. Stobinski L, Lesiak B, Kövér L, Tóth J, Biniak S, Trykowski G, Judek J (2010) J Alloys Compd 501:77–84
89. NIST X-ray Photoelectron Spectroscopy Database (2012) U.S. Secretary of Commerce. https://www.srdata.nist.gov/xps/. Accessed 13 June 2017
90. Lesiak B, Stobinski L, Malolepszy A, Mazurkiewicz M, Kövér L, Tóth J (2014) J Electron Spectrosc Relat Phenom 193:92–99
91. Chandrasekharan N, Kamat PM (2000) J Phys Chem B 104:10851–10867
92. Varghese OK, Paulose M, LaTempa TJ, Grimes CA (2009) Nano Lett 9:731–737
93. Baltrusaitis J, Schuttlefield J, Zitler E, Grassian VH (2011) Chem Eng J 170:471–481
94. Wu Z, Jiang D, Mann AKP, Mullins DR, Qiao Z, Allard LF, Zeng C, Jin R, Overbury SH (2014) J Am Chem Soc 136:6111–6122
95. Turner VB, Golovko OPH, Yaughan P, Abdulkin A, Brenguer-Murcia MS, Tikhov BFG, Lambert RM (2008) Nature 454:981–983
96. Yang MX, Jo SK, Paul A, Avila L, Bent BE, Nishikida K (1995) Surf Sci 325:102–120
97. Burchan LJ, Wachs IE (1999) Catal Today 49:467–484

Affiliations

Balázs László[1] · Kornélia Baán[1] · Albert Oszkó[1] · András Erdőhelyi[1] · János Kiss[3] · Zoltán Kónya[2,3]

[1] Department of Physical Chemistry and Materials Science, University of Szeged, Aradi vértanúk tere 1., Szeged 6720, Hungary

[2] Department of Applied and Environmental Chemistry, University of Szeged, Rerrich Béla tér 1., Szeged 6720, Hungary

[3] MTA-SZTE Reaction Kinetics and Surface Chemistry Research Group, Rerrich Béla tér 1., Szeged 6720, Hungary